ACS APPLIED NANO MATERIALS

Article

4D Imaging of ZnO-Coated Nanoporous Al$_2$O$_3$ Aerogels by Chemically Sensitive Ptychographic Tomography: Implications for Designer Catalysts

Hao Yuan, Hui Yuan, Travis Casagrande, David Shapiro, Young-Sang Yu, Bjoern Enders, Jonathan R. I. Lee, Anthony van Buuren, Monika M. Biener, Stuart A. Gammon, Theodore F. Baumann, and Adam P. Hitchcock*

Cite This: *ACS Appl. Nano Mater.* 2021, 4, 621–632

Read Online

ACCESS | Metrics & More | Article Recommendations | Supporting Information

ABSTRACT: The 3D chemical structure (4D spectromicroscopy) of nanoporous Al$_2$O$_3$ aerogels coated with ZnO by atomic layer deposition (ALD) was studied by multienergy scanning transmission X-ray microscopy. These materials are representative of a class of designer catalysts in which the nanoporous support is prepared separately from the active catalyst material, which is subsequently introduced by ALD, thereby allowing independent optimization of the morphology, chemistry, and spatial distribution of the support and catalyst. The samples studied were prepared by Ga ion and Xe plasma focused ion beam (FIB) milling as well as drop casting from water suspension. Zn L and Al K edge spectra of six samples with three different ZnO loadings were measured to investigate how loading and different sample preparation methods affect the 3D distribution of the ZnO and Al$_2$O$_3$. Scanning transmission X-ray microscopy (STXM) and ptychographic imaging at two energies each at the Zn L$_3$ and Al K edge were measured. The ptychography data were analyzed by using the SHARP reconstruction code to generate quantitative 2D chemical maps of the Al$_2$O$_3$ and the ZnO. The STXM and ptychography maps were then measured at a sequence of tilt angles, covering up to 160° of rotation. The 3D structure of the ZnO and Al$_2$O$_3$ was derived from the tilt series data by tomographic reconstruction using a compressed sensing algorithm. A two-dimensional spatial resolution (half-period) of 6 nm, measured by Fourier ring correlation, and a 3D spatial resolution (half-period) of 9 nm, measured by Fourier shell correlation, were achieved when using the COSMIC beamline at the Advanced Light Source (ALS). The results show that for all of the ZnO loadings studied there is nonuniform coverage of the ZnO on the Al$_2$O$_3$ aerogel framework. In addition, we found that both FIB methods create sample artifacts, although the distortion was less with Xe plasma than Ga ion FIB.

KEYWORDS: ptychography, X-ray spectromicroscopy, tomography, atomic layer deposition, aerogel
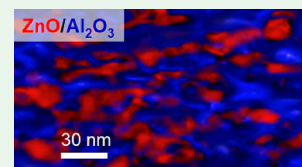
1. INTRODUCTION

Multicomponent nanoporous materials with optimized functionality are of increasing importance in energy conversion and catalysis. By adjusting pore size and connectivity of a substrate and adding coating material(s) with controlled thickness, spatial distribution, and overall density, we can optimize these composite materials for specific applications. Previous work has demonstrated the utility of atomic layer deposition (ALD) on porous aerogel substrates to create functional heterostructured materials.[1−3] However, our understanding of the deposition process, and thus optimization of ALD, is currently incomplete.[3] 4D imaging—chemically specific, quantitative 3D mapping—of the nanostructure of nanoporous, ALD-coated aerogels can provide insight into their physical and chemical properties, thus improving the ability to prepare materials where both the substrate and the active species are optimized for a particular function.

Four-dimensional (4D) imaging[4] is a powerful approach for characterizing the physical and chemical properties of heterostructured systems. Soft X-ray ptychography[5] is a coherent diffraction imaging technique readily implemented in scanning X-ray transmission microscopes (STXM).[6] By measuring spectro-ptycho-tomography—2D ptychographic images at multiple photon energies and multiple tilt angles—we can derive the 3D distributions of multiple chemical species. Our previous ptycho-tomography study[7] of a nanoporous Al$_2$O$_3$ aerogel substrate with an ALD ZnO coating demonstrated the power of chemically selective ptycho-tomography to determine the chemical state and 3D structure of samples and achieved a 2D spatial resolution (half-period) of 14 nm. The much-increased coherent flux at the COSMIC beamline at the Advanced Light Source (ALS, Berkeley Lab),[8] and improvements to the SHARP ptychographic reconstruction software,[9]
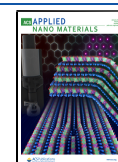
have dramatically improved soft X-ray ptychography capabilities. In this work, we present an extended chemically selective, ptycho-tomography study of six different ZnO ALD-coated Al_2O_3 aerogel samples prepared using three different ALD loadings of ZnO. A 2D spatial resolution (half-period) of 6 nm, measured by Fourier ring correlation, and a 3D resolution of 9 nm, measured by Fourier shell correlation, were achieved by using the COSMIC beamline and endstation.

This paper is organized as follows. Section 2 describes experimental acquisition and data analysis methods. Section 3 presents our results: first STXM 2D chemical imaging, then STXM spectroscopy, then ptychography 2D and 3D imaging, followed by evaluation of the ptychographic spatial resolution in 2D and 3D. The discussion (section 4) starts by evaluating sample damage by the different focused ion beam (FIB) procedures used and possible X-ray damage. It then compares the different ZnO ALD loadings (6-, 12-, and 25-cycle) and sample preparations with respect to quantitation of amounts, uniformity of aerogel coverage, and particle sizes. In addition to demonstrating the significant improvement in spatial resolution provided by the new COSMIC ptychography facility at the ALS (relative to earlier ptychography measured by using different beamlines at the ALS), these results give a systematic picture of how the structure of ZnO ALD coated on Al_2O_3 evolves with increasing numbers of ALD cycles.
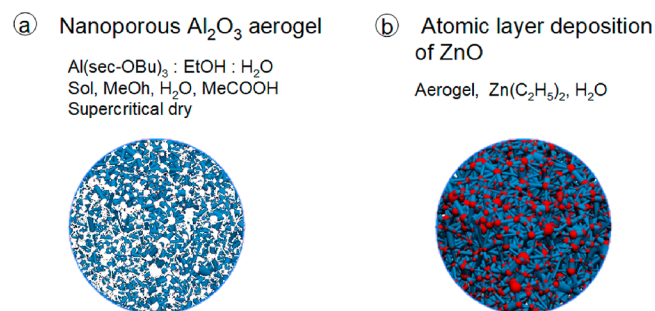
2. EXPERIMENTAL SECTION

2.1. Sample Preparation. To understand the ALD processing and its effect on the final nanostructure of the Al_2O_3 aerogel, three ZnO-coated aerogels with different ALD layers, 6, 12, and 25 cycles, were prepared by using the same preparation procedures. Different methods for preparing the samples for X-ray microscopy (water casting, Ga and Xe plasma FIB milling) have been used. Samples were measured with both STXM at CLS and soft X-ray ptychography at beamline (BL) 5.3.2.1 and COSMIC BL 7.0.2 at the ALS. Details of the samples and measurements are summarized in Table S1.

As outlined in Scheme 1, the alumina aerogel was prepared by using a two-step sol−gel process.[10] Following supercritical drying, the monolith aerogel had a bulk density of ~100 kg/m³, about 40 times less than that of bulk Al_2O_3 (4×10^3 kg/m³).[10,11] The alumina aerogel was then ALD-coated with 6, 12, or 25 cycles of ZnO. Each cycle consisted of diethylzinc ($ZnEt_2$) and H_2O precursor half-cycles in a warm wall reactor (wall and stage temperature of 110 °C).[1] In the second ALD half-cycle, long pump (20 s), pulse (500 s at ~133 Pa), and nitrogen purge (500 s) steps were used to promote uniform coating throughout the porous material. To facilitate handling, the aerogels were kept in their molds during the whole ALD coating process.

The samples measured by STXM spectromicroscopy and ptychographic spectrotomography were prepared by three different methods.

(i) Water casting: An aerogel sample was crushed by using a clean scalpel blade and then dispersed in distilled water to obtain a low concentration dispersion of aerogel powder. A small drop of the dispersion was dropped on a Formvar-coated TEM grid and air-dried. After drying, a single grid strip with the region of interest was excised by a scalpel.

(ii) Ga FIB: Two different Ga FIB preparations were made, with the second one designed to significantly reduce the ion beam dose to the sample, which was thought to be the source of significant ZnO depletion in the outer few micrometers of the first Ga FIB preparation.[7] In the first preparation (Ga-FIB#1), a 5 nm carbon layer was deposited on a section of the aerogel for electrical conduction. The sample was then Ga FIB milled into a $20 \times 30 \times 30$ μm³ rectangular prism and mounted at the tip of a strip of TEM grid. In the second preparation (Ga-FIB#2), a 10 μm long conical−cylindrical sample with a diameter varying from 3 to 4 μm tip to base was formed to be similar in shape to the Xe-FIB#2

Scheme 1. Preparation of ZnO-Coated Alumina Aerogels[a]

[a](a) Two-step sol−gel synthesis of nanoporous aluminum oxide. Step 1: aluminum *sec*-butoxide, ethanol, water mixture {Al(*sec*-OBu)₃:EtOH:H₂O = 1:16:0.6 molar} was heated to 60 °C and stirred for 45 min. Step 2: after cooling to room temperature (RT), a 99% porous gel was made by stirring a mixture of the sol, methanol, water, and acetic acid {Sol:MeOH:H₂O:CH₃COOH = 1:0.2:0.003:0.03 mass} for 30 min at RT and then letting the aerogel set for 2 h in a mold. The gel was then dried by rapid supercritical extraction of methanol in an autoclave. (b) Atomic layer deposition of ZnO: multiple (6, 12, or 25) cycles, each cycle consisting of (i) deposition of diethylzinc (ZnEt₂) and H₂O precursor in a warm wall reactor at 110 °C; (ii) pump (20 s), pulse (500 s at ~133 Pa), and N₂ purge (500 s).

sample. The preparation methods of Ga-FIB#2 were intended to reduce ion beam damage effects compared to Ga-FIB#1. The key changes for preparing Ga-FIB#2 were (a) the aerogel particle was attached to the TEM grid prior to any FIB trimming, (b) a thin carbon layer was electron beam deposited followed by a 1 μm thick ion beam deposited carbon protection layer, (c) the conical−cylindrical shape was milled with the ion beam nearly parallel to the long axis of the cylinder to minimize the ion beam penetration depth, and (d) the dose from ion beam imaging throughout the process was minimized by using low ion current and minimal imaging. The trimming of Ga-FIB#1 into a rectangular prism required ion beam imaging perpendicular to the sample faces, so the Ga penetration depth was much larger compared to the conical cylinder of Ga-FIB#2.

(iii) Xe plasma focused ion beam (PFIB): Three different samples were made by Xe plasma FIB. In the first case (Xe-FIB#1), after electron beam depositing a 1 μm thick layer of C + Pt on the sample, another 3 μm C + Pt layer was ion beam deposited on the aerogel to protect the region of interest from ion bombardment induced damage during the milling process. A rectangular prism was then lifted out, transferred to a Cu grid, and trimmed to 5 μm × 5 μm × 10 μm by using 30 kV and 100 pA (2.8×10^{-9} pC/μm², as reported by the FIB control software). For the second and third preparations (Xe-FIB#2 and Xe-FIB#3), the material was prepared in a similar manner, and then a section of about $10 \times 10 \times 15$ μm³ was lifted out and transferred to a post on a FIB half grid. It was then trimmed to an ~3.5 μm diameter conical−cylindrical shape ~10 μm long by milling with gradually decreased ion beam currents at a 30 kV accelerating voltage. Finally, the milled sample was cleaned by using a Xe plasma beam at 8 kV, 100 pA (2.8×10^{-9} pC/μm²). Throughout both the Ga FIB and Xe PFIB preparation processes, the electron beam acceleration voltage and current were kept to a minimum to reduce electron beam damage effects[12] on this beam-sensitive material. In general, both the electron and ion beam parameters used were chosen to minimize thermal effects and electronic or knock-on damage.[13−15]

2.2. Data Acquisition. Ptychography measurements were performed at the Advanced Light Source (ALS) while STXM was performed at the ALS and the Canadian Light Source (CLS). Details of the beamline used, timing, and conditions of the measurements for each

sample are summarized in Table S1. STXM data were measured at ALS BL 11.0.2 and at CLS 10ID1 ambient STXM. STXM and ptychography studies were performed by using Nanosurveyor 1[16] on ALS BL 5.3.2.1[5,17] and Nanosurveyor II[18] at the COSMIC beamline 7.0.1.2[19] at the ALS.

2.2.1. STXM Spectromicroscopy at CLS and ALS. In general, spectroscopy was measured in areas adjacent to the area used for ptychography. Spectra were recorded by using the STXM stack mode,[20] with a variable point spacing which is described in footnotes to Table S1. The transmission mode stacks were aligned and converted to optical density (OD) by using I_0 measured off the sample but through space (for FIB samples) or the Formvar support (in the case of water-cast samples), and the spectra were extracted from suitable areas. The energy scales were set by using values reported in the literature. The first feature in the Zn L_{23} spectrum was calibrated to 1024.1 eV,[21−23] and the second peak in the Al K spectrum was calibrated to 1568.0 eV.[24−28] Quantitative OD1 spectra[6] (response for 1 nm of pure ZnO or Al_2O_3) were derived by matching spectral shapes and intensities below and far above each edge to the response predicted from the elemental compositions from standard mass absorption coefficient tabulations[29] and the density of bulk ZnO (5.61 g cm^{-3}) and Al_2O_3 (3.95 g cm^{-3}). These OD1 spectra were then used for quantitative analysis. Images at two energies (called a stack map) were used to measure the distributions of ZnO ($OD_{1027} − OD_{1015}$ or $OD_{1050} − OD_{1015}$) and Al_2O_3 ($OD_{1568} − OD_{1550}$) in the ZnO/Al_2O_3 aerogel samples. All data processing was performed by using aXis2000.[30]

2.2.2. Beamline 5.3.2.1 Ptychography. The first ptychographic tomography measurements, reported elsewhere,[7] were performed on the water-cast sample A by using the Nanosurveyor I endstation at the 5.3.2.1 bend magnet beamline at the ALS. A zone plate (ZP) with outer zone width of 60 nm was used. The sample was raster scanned through the ∼75 nm focus spot with a step size of 50 nm. A custom-built high-frame-rate CCD detector[31] was used to record diffraction images with a single point exposure time of 150 ms. Ptychographic images were measured at 1010 and 1026.8 eV (below and above the Zn L_3 edge, respectively). For tomography, these image pairs were recorded at 14 tilt angles, from −65° to +65° with a step size of 10°. The ptychography measurements were only performed at the Zn L-edge because the coherent flux at the Al K-edge (1570 eV) in the 5.3.2.1 bend magnet beamline was too low. In addition, at the time of these measurements, a Si foil was installed to attenuate the bright field portion of scattering patterns on the detector. For energies below 1200 eV, this reduced the intensity of the bright-field signal to a level allowing a single time exposure. However, the Si foil was overly transparent at the Al K-edge, resulting in saturation of the bright field at exposure times sufficient to detect the dark-field coherent scattering signal. As outlined in our earlier publication,[7] a 2D spatial resolution (half-period) of 14(2) nm was achieved.

2.2.3. ALS COSMIC Ptychography. Ptychographic measurements were performed by using the Nanosurveyor II (NS-II) endstation[18] at the COSMIC beamline (7.0.1.2) at the Advanced Light Source (ALS). A 360 μm diameter zone plate with an outer zone width of 45 nm (produced by the Centre for X-ray Optics, Berkeley Lab) was used. In NS-II the zone plate is scanned. After setting the sample z-position to focus, the ZP was raster-scanned by using a step size of 40 nm. The fast DoE CCD detector,[31] cooled to −50 °C by a low-temperature immersion chiller, was used to record diffraction images with two sequential exposures: a 10 ms short exposure in which the bright-field signal is not distorted by detector saturation, but the dark-field diffraction signal is recorded with inadequate statistics, followed by a 100 ms long exposure in which the detector response is totally saturated in the bright-field area but the dark-field diffraction signal is recorded with better statistics. In some cases (samples F, F′, and H), a single exposure of 10 ms was also used. No filter was used. Ptychographic data, typically over a 4 μm × 5 μm area (values for March 2019), were measured at four energies: the Zn L_3 pre-edge and above edge signal (1015 and 1050 eV) and the Al K pre-edge and absorption peak (1550 and 1568 eV). These stack maps were measured at 14 tilt angles, from −65° to +65° with a step size of 10°. At each energy point and tilt angle, the camera background signal was measured with the beamline shutter

closed, and that background was removed from each CCD image in subsequent data processing. The four images measured at each angle were combined and aligned to compensate for small drifts (∼100 nm over 2 h). At each new angle the field of view was adjusted in the few micrometers scale to accommodate imperfect alignment of the sample rotation axis and the X-ray beam.

2.3. Ptychographic Reconstruction. Ptychographic images were reconstructed by using the relaxed averaged alternating reflection (RAAR) reconstruction algorithm implemented in the SHARP ptychography code (ver. 9.0.7) developed by the Center for Applied Mathematics for Energy Research Applications.[9] A total of 500 iterations were applied to ensure convergence to a high-quality ptychographic reconstruction (see Figure S1). Prior to reconstruction, the effect of isolated beam intensity fluctuations between diffraction exposures (due to top-off injections or other transient sources) was reduced by calculating the equivalent STXM image from the integrated diffraction signal at each scan position and then comparing it to a median filtered version of the same image. Diffraction frames that deviated significantly were rescaled according to the filtered value. In addition, a probe mask was used to reduce artifacts associated with rectilinear scanning. The optical density (OD) of a complex valued ptychography reconstruction is calculated as $−\ln(|P|/\langle|P_0|\rangle)$, where $|P|$ is the modulus of the complex valued image and $\langle|P_0|\rangle$ is the spatial average of the modulus of complex values in the region unobstructed by the sample. The four ptychography images measured at each tilt angle were aligned by using the stack analyze alignment routine (Jacobson), implemented in aXis2000.[30] Quantitative 2D chemical distributions were derived from the difference between the ptychography absorption images at the pre-edge and above-edge energies. To obtain quantitative signals the differential response $[(OD_{1050} − OD_{1015})$ for ZnO and $(OD_{1568} − OD_{1550})$ for $Al_2O_3]$ was scaled to the corresponding $\Delta OD1$ response in the Zn L_{23} OD1 spectrum of ZnO and the Al K-edge spectra OD1 spectrum of Al_2O_3 (see Figure S2).

2.4. Tomographic Reconstruction and 3D/4D Visualization. For the ptychographic tomography measurements, rough alignment was performed manually in the Dragonfly software.[32] The Dragonfly alignment was followed by an auto affine transformation in ImageJ[33] to correct for global shearing or localized image distortions caused by thermal drifts or mechanical issues. aXis2000 was then used to convert the angle stack files for the ZnO and Al_2O_3 components to mrc format. A compressed sensing (CS) algorithm[34] was then used for the tomographic reconstruction. CS reconstruction methods, which are more robust than alternatives such as the simultaneous iterative reconstruction technique (SIRT), provide excellent reconstruction quality even when a very small number of tilt angles are used and there is a significant missing wedge.[34] The 3D volume reconstruction data were then segmented and rendered for 3D chemical visualization by using Dragonfly software.[32]

3. RESULTS

3.1. STXM Overview of the Xe FIB#1 Sample. Figure 1a presents a scanning electron microscope (SEM) image of sample F (Xe-FIB#2). Figure 1b is a STXM OD image at 1050 eV (in the Zn 2p ionization continuum). Figure 1c is a STXM OD image at 1568 eV at the peak of the Al 1s spectrum. Figure 1d is a composite of the Al_2O_3 (blue) and ZnO (red) maps derived from two energy stack maps, color-coded by the thickness in nanometers, determined by taking the ratio of the difference in OD at the above- and below-edge energies to that of the difference in the OD1 values at the same two energies (see Figure S2), where OD1 is the OD of ZnO or Al_2O_3 at standard density and a thickness of 1 nm.

The area at the tip of the sample is bright in single energy images like Figures 1b and 1c because it is dense material with an OD much larger than the upper OD limit of the gray scale used. Because the tip does not contain either Zn or Al, the component maps derived from the (on−off) edge signals are featureless. The
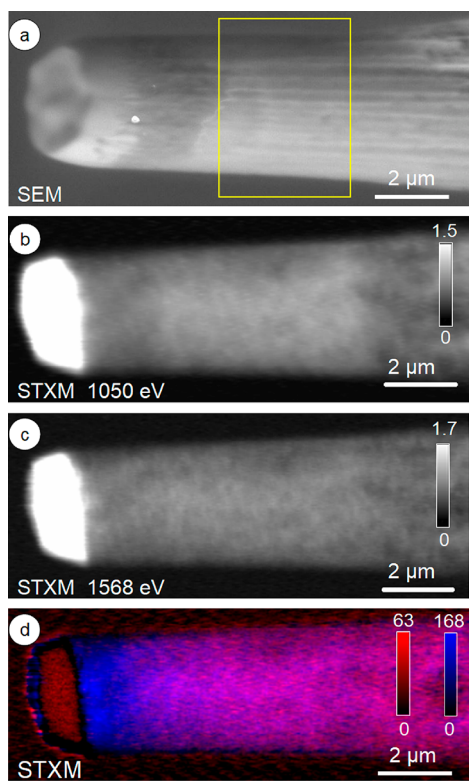
Figure 1. (a) SEM image of a Xe plasma FIB milled ZnO ALD-coated Al_2O_3 aerogel sample (Xe-FIB#2, sample F). The region examined by chemically selective ptycho-tomography is indicated by the yellow box. (b) STXM OD image at 1050 eV (Zn L_3 continuum). (c) STXM OD image at 1568 eV (Al K peak). (d) Rescaled, color-coded composite of the STXM maps of Al_2O_3 ($OD_{1568} - OD_{1550}$, red) and ZnO ($OD_{1050} - OD_{1015}$, blue). The gray scales in (b, c) indicate optical density (OD). The red and blue color scales indicate the thickness in nm of the ZnO (red) and Al_2O_3 (blue), derived from $\Delta OD/\Delta OD1$, the ratio of the differential optical density (ΔOD) to the differential optical density ($\Delta OD1$) for 1 nm of the chemical species at its standard density (COSMIC, March 2019).

Zn L and Al K stacks were measured from the part of the sample at the right side of the viewed area, while the ptychography stack maps and tilt-angle data were measured in the area in the yellow box in Figure 1a.

3.2. STXM Spectroscopy. Figure 2 compares the Zn L_3-edge (2p) and Al K-edge (1s) X-ray absorption spectra of the three different ZnO ALD preparations that were studied. The Zn L-edge spectra (Figure 2a) and Al K-edge spectra (Figure 2b) of 6-cycle spectra is the average of the spectra of samples D, E, and G; the 12-cycle spectra are from sample H, and the 25-cycle spectra are from sample A. The spectra of sample D (Ga-FIB#1) were presented earlier.[7] Although all spectra were measured from ZnO-coated Al_2O_3 aerogels and thus are mixtures, the spectra of the individual chemical components can be derived with reliability because the absorption edges are sufficiently far apart in energy that the contribution of alumina to the Zn L-edge spectra is a smoothly declining curve, as is the contribution of zinc oxide to the Al K-edge spectra. The spectrum of pure ZnO was isolated from the spectrum of the aerogel sample by subtracting a scaled version of the elemental response spectrum (OD1) of Al_2O_3 from the Zn L_{23} region, whereas the spectrum of pure Al_2O_3 was obtained by subtracting a scaled version of the elemental response spectrum (OD1) of
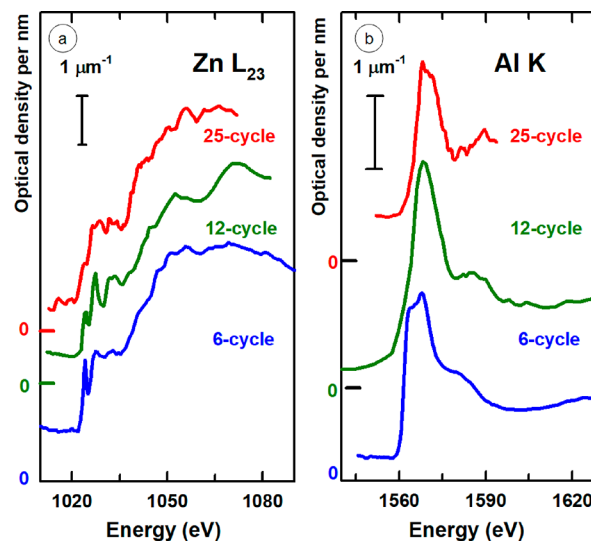

Figure 2. (a) Zn L-edge and (b) Al K-edge spectra of the 6-, 12-, and 25-cycle ZnO ALD-coated Al_2O_3 aerogel samples. The spectra of samples D, E, and G were averaged for the 6-cycle spectra, while the 12-cycle spectra are those of sample H and the 25-cycle spectra are those of sample A. The spectra have been energy calibrated and are reported on an absolute intensity scale, with the indicated offsets; see the text for details (multiple runs on different synchrotron facilities and beamlines).

ZnO from the Al K-edge region. The resulting OD1 spectra of the pure species are presented in Figure S2.

The spectra of the 6-, 12-, and 25-cycle ZnO ALD preparations (Figure 2a) are quite similar, although some differences in the near-edge structure are apparent. The Zn L-edge spectrum of ZnO has been presented previously.[21,23,35] The spectra presented in Figure 2a are in reasonable agreement with the published spectra. The characteristic ZnO L_3 spectral features are a "triplet" at 1022.5, 1024.1, and 1030.2 eV and an additional peak at 1033 eV, all of which arise from excitations of Zn 2p electrons to unoccupied Zn 4s and Zn 4d states. The Al K-edge spectra of α-Al_2O_3 (corundum), other Al_2O_3 allotropes, and alumina silicates have been presented previously.[24,28,36−38] In this case there is a large variability in Al K-edge spectra, depending on the crystal structure. Several authors have noted a significant correlation between Al K-edge spectral shape and position and the relative proportion of octahedral ([6]-Al) and tetrahedral ([4]-Al) sites.[24,36] In general, the main Al 1s → 3p transition intensity in Al(III) oxidation state species in either the pure oxides, aluminosilicate minerals, or zeolites occurs around 1566.5 eV for tetrahedral ([4]-Al) sites and about 2 eV higher, around 1568.5 eV, in octahedral ([6]-Al) sites. Figure S3 compares the Al K-edge spectra of the ZnO/Al_2O_3 aerogel species to the spectra of corundum (α-Al_2O_3), in which all the Al are in AlO_6 environments: mordenite, an aluminosilicate zeolite in which all the Al is in AlO_4 environments, and θ-Al_2O_3 in which there is a 50:50 ratio of AlO_4 and AlO_6 environments. For the reference compounds, as the structure gets more complex, the envelope of transitions increases. The Al K-edge spectrum of the ZnO ALD-coated Al_2O_3 aerogel is very broad and shows a number of indistinct shoulders in the corresponding energy region. This suggests that the alumina of the aerogel material has a wide range of local structures and is noncrystalline, as was concluded in our earlier study.[7]

Figure 2 presents the Zn L and Al K spectra on an OD1 scale (response per nanometer thickness), which masks the

quantitative compositional information accessible in an OD scale. The ratio of amounts of ZnO to Al_2O_3, averaged over the volumes imaged, was derived from the quantitative STXM data. These values are summarized in Table S2. The dependence of the derived composition on the number of ALD cycles and sample preparation method are discussed in detail below.

3.3. 2D Imaging and Chemical Mapping. Figures 3a and 3c show chemically specific 2D projection maps of the Al_2O_3 and
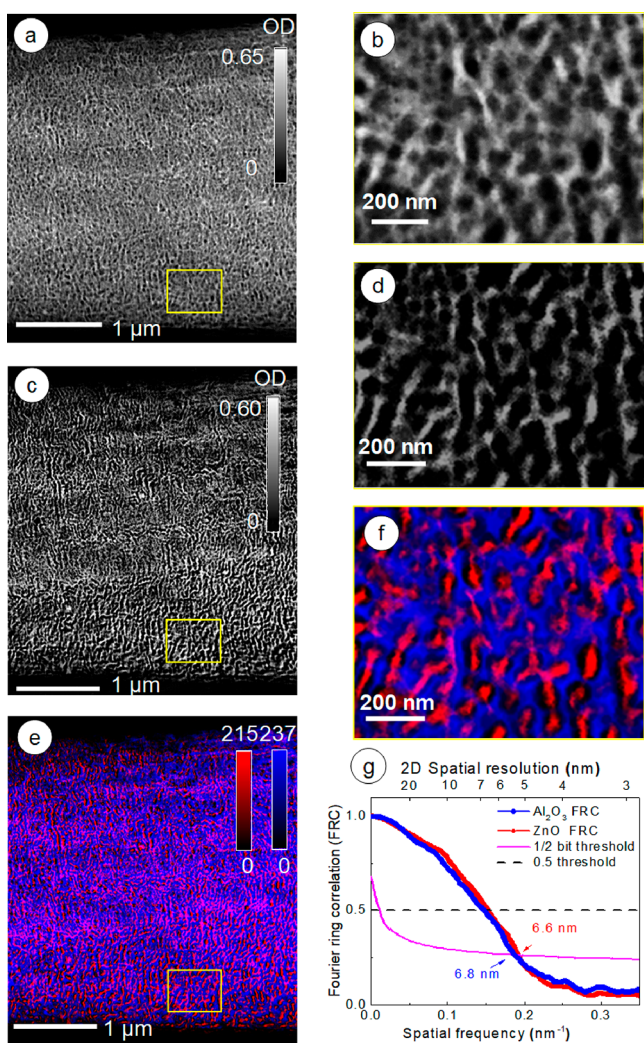

Figure 3. 2D chemical maps of a 6-cycle ZnO/Al_2O_3 aerogel sample (Xe-FIB#2, sample F) derived from reconstructed ptychography amplitude images. (a, b) Al_2O_3 ($OD_{1568} - OD_{1550}$), (c, d) ZnO ($OD_{1050} - OD_{1015}$). The gray scale indicates the difference in optical density. (e, f) Color-coded composite map of ZnO (red)/Al_2O_3 (blue). The color scales indicate thickness in nm from $\Delta OD/\Delta OD1$. (b, d, f) are expansions of (a, c, e) in the same area at the edge of the sample. (g) Two-dimensional (2D) spatial resolution of ptychographic imaging estimated from a Fourier ring correlation (FRC) analysis of the Al_2O_3 and ZnO ptychography reconstructed 2D chemical maps (a, b) of sample F (COSMIC, March 2019).

ZnO distributions in the Xe plasmaFIB#2 sample F, each derived from two ptychography images reconstructed with a pixel size of 5.2 nm. These maps are derived from ptychography amplitude signals, converted to absorption, and subtracted. The limits of the optical density difference gray scale are indicated. Figures 3b and 3d are expanded areas of the lower center region of the area measured, which show the structure in greater detail.

The Al_2O_3 aerogel structure is a relatively uniform porous network (Figure 3a). The ZnO distribution (Figure 3c) is superficially similar but is less uniform and more "patchy". Figure 3e is a rescaled color composite of the Al_2O_3 (blue) and ZnO (red) signals. The red and blue scales indicate thickness in nanometers, where the thickness is that the material would have at standard density for ZnO and Al_2O_3. Figure 3f is the expanded area of Figure 3e. In Figures 3e and 3f the purple pixels correspond to columns where there is both ZnO and Al_2O_3. The existence of relatively pure red and blue areas, in addition to purple, indicates that the ZnO coating is nonuniform.

3.4. 3D Tomography Reconstruction. 3D spatial distribution maps of the two chemical components are needed to visualize the distribution of the ZnO coating on the Al_2O_3 substrate. Figure 4a and Movie S1 present a rendering of the
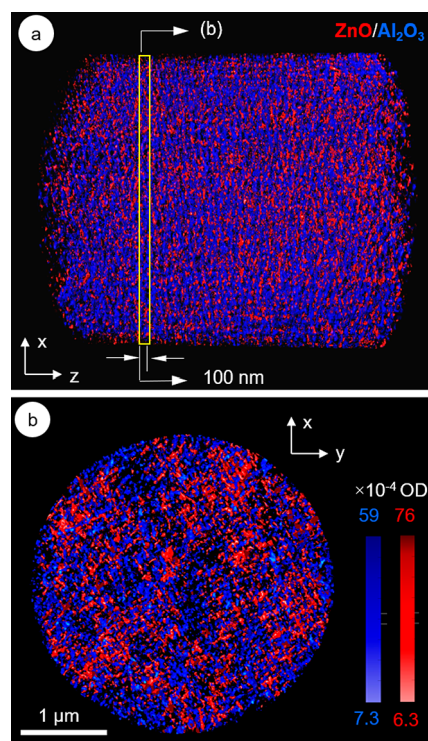

Figure 4. (a) Volume rendering of the Al_2O_3 (red) and ZnO (blue) chemically selective 3D distributions from ptycho-tomography of a Xe plasma FIB-milled ZnO/Al_2O_3 sample (Xe-FIB#2, sample F). Otsu thresholds of 7.3×10^{-4} (OD/voxel) for Al_2O_3 and 6.3×10^{-4} for ZnO were used. (b) 100 nm cross-section slice cut through the position indicated by the yellow rectangle in (a). (COSMIC, March 2019).

rescaled color-coded composite of the 3D reconstructed Al_2O_3 (blue) and ZnO (red) volume signals of sample F with voxel size of $5.2 \times 5.2 \times 5.2$ nm^3. Otsu thresholds[39] of 7.3×10^{-4} (Al) and 6.3×10^{-4} (Zn) were used. The porosity of the entire volume ($57 \pm 2\%$) was calculated by using the Bone Analysis plug-in tool in Dragonfly.[32] The volume fraction of Al_2O_3 is $25 \pm 1\%$ and ZnO is $18 \pm 1\%$. Figure 4b shows a 100 nm thick slice from the center of the 3D volume. This indicates that the ZnO ALD coating is not uniformly distributed on the Al_2O_3 framework structure. We also found ~10% depletion of ZnO in the outer 200 nm of the pillar (see Figure S4) probably caused by modification of the sample by the Xe plasma beam. We expect that ZnO would be preferentially sputtered relative to Al_2O_3 and the Xe plasma beam would penetrate a significant depth into the

highly porous aerogel. The ZnO depletion at the surface of the FIB pillar was higher for samples prepared by Ga FIB than Xe plasma FIB (see Figure S4 and ref 7).

Figure 5a displays a 30 nm thick slice cut from the Al_2O_3 3D map derived from the reconstructed chemically selective ptycho-
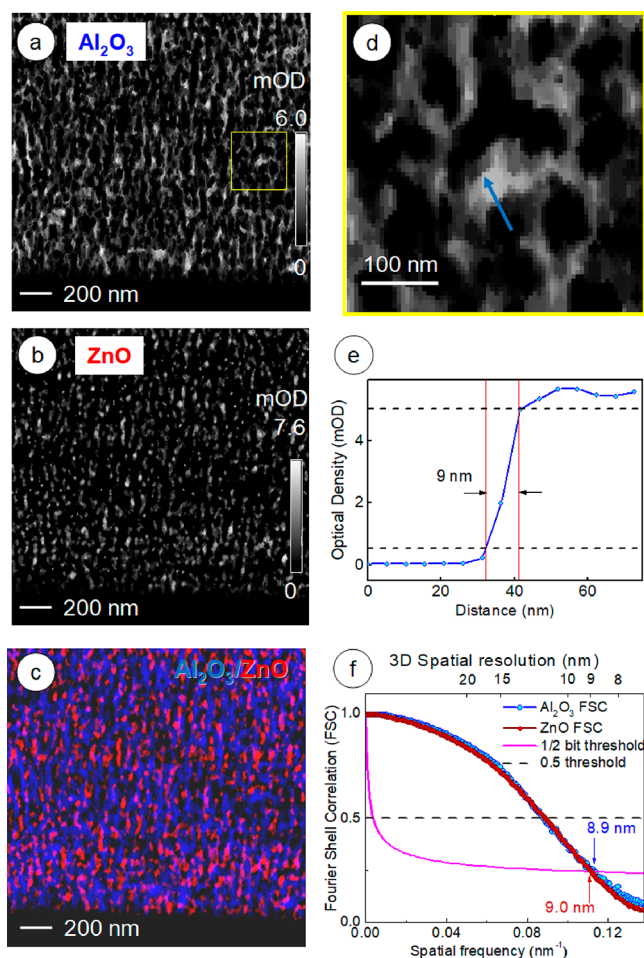

Figure 5. (a) 30 nm slice from the Al_2O_3 3D map extracted from the tomographic reconstruction of the multienergy ptychography of the ZnO/Al_2O_3 sample (Xe-FIB#2, sample F). (b) ZnO 3D map in the same 30 nm tomography reconstruction slice. (c) Color-coded composite of the Al_2O_3 (blue) and ZnO (red) maps. (d) 10 nm slice of Al_2O_3 ptychography map in the region of the yellow box in (a). (e) Intensity profile across the indicated line in (d) used to estimate the 3D spatial resolution. The black dashed lines are guides for the 10−90% spatial resolution criteria. (f) Three-dimensional (3D) spatial resolution estimated from a Fourier shell correlation (FSC) analysis of the 3D Al_2O_3 and ZnO ptychography tomography reconstruction (Figure 4) (sample F) (COSMIC, March 2019)

tomography data for sample F. Figure 5b is the ZnO map from the same 30 nm thick slice. In contrast to the linked "ribs" of the highly porous Al_2O_3 aerogel, the ZnO signal in the slice is in the form of discrete, quasi-circular "dots". High-resolution TEM of the 25-cycle sample previously showed these are 10−20 nm ZnO single crystals.[7] Figure 5c is a color-coded composite of the Al_2O_3 (Figure 5a) and ZnO (Figure 5b) component maps. The essentially pure red (ZnO) and pure blue (Al_2O_3) colors indicate there is negligible mixing. If the ZnO was actually perfectly conformal, the presence of both ZnO and Al_2O_3 in the same volume would lead to a composite map with mostly shades of purple. Thus, the map in Figure 5c clearly shows that the ZnO

(red) is not conformal (as expected for an ideal ALD), but rather present as roughly spherical particles, irregularly attached to the Al_2O_3 porous structure (red). This structural conclusion is consistent with the results of our previous, lower resolution, chemically selective ptycho-tomography study.[7] The present analysis is much more convincing on account of the higher spatial resolution. Figure 5d plots an expanded representative area of the Al_2O_3 map indicated by the yellow square in Figure 5a, which shows the Al_2O_3 signals in more detail. The profile across the edge of the Al_2O_3 "rib" indicated by the blue line in Figure 5d is plotted as a line profile in Figure 5e. A knife-edge analysis of the intensity line profile yields an estimated 3D spatial resolution of 9 nm.

Figure S5 shows ptychographic 2D projection and 3D tomographic reconstruction results from the 12-cycle ALD aerogel, sample H, with a pixel size of 4.8 nm and voxel size of 4.8^3 nm^3, respectively. Unfortunately, that sample was damaged in the process of introducing it into the COSMIC microscope. Despite that, it was possible to measure ptychographic maps and tomography data sets and do a sufficiently high-quality ptychography reconstruction, alignment, and tomographic reconstruction to obtain meaningful results.

Movie S1 is a color-coded composite of the ZnO and Al_2O_3 ptycho-tomography reconstructions. It shows the 3D chemical distribution and structure of the composite from a number of angles and fields of view and with a cut-through view.

3.5. Evaluating Ptychography Resolution in 2D and 3D. As used previously,[7] the spatial resolution of the 2D ptychography chemical maps (Figure 3a,b) was evaluated by using the Fourier ring correlation (FRC) method[40] which gives estimates of the half-period resolution. The results for 2D spatial resolution are displayed in Figure 3g. The FRC analysis of the Al_2O_3 map indicates a spatial resolution of 6.8 nm by using the 0.5 threshold or 5.3 nm by using the half-bit threshold. For the ZnO ptychographic stack map, a spatial resolution of 6.6 nm (0.5 threshold) or 5.2 nm (1/2-bit threshold) is indicated via FRC analysis. This is a significant improvement compared to the 14 nm spatial resolution achieved with the earlier ptychography studies at beamline 5.3.2.1.[7] We attribute this improved spatial resolution primarily to the much higher coherent flux at the COSMIC beamline which provides a clearer visualization of the spatial distribution of the ZnO ALD coating on the Al_2O_3 porous framework. Figure S6 compares the 2D spatial resolution achieved in earlier chemically selective ptycho results on the same type of sample, but water cast, by using ALS bend magnet BL 5.3.2.1[7] with that achieved by using on sample E via the COSMIC beamline. A significant improvement in spatial resolution was achieved. The 2D spatial resolution of individual ptychographic images was in the 5−7 nm range for each of three different COSMIC runs.

The 3D spatial resolution of the tomographic reconstruction of sample F was analyzed by the Fourier shell correlation (FSC) method.[41] The results are shown in Figure 5f. The FSC analysis indicates a spatial resolution (half-period) of 9.0 nm for the ZnO structure and 8.9 nm for the Al_2O_3 frame. Note that the actual 3D resolution is likely somewhat higher since FSC reduces the signal-to-noise ratio of the data by a factor of 2 at all spatial frequencies.[42] A 3D spatial resolution of 9 nm was also deduced from the sharpness of the intensity line profile (Figure 5e). A slight improvement (∼2%) in the 3D spatial resolution was observed by increasing the number of iterations of the CS tomographic reconstruction from 50 to 200 (see Figure S7), but this did not affect the main conclusions of the analysis. The 3D

spatial resolution of these COSMIC ptycho-tomography results (~9 nm) is significantly better than the 3D spatial resolution of ~30 nm achieved by using other ALS beamlines in our previous investigation.[7]

4. DISCUSSION

4.1. Sample Damage by Focused Ion Beams and X-rays. Focused ion beams are designed to remove material by ion bombardment. It is known that interactions of the ion beam and the sample can selectively modify chemical composition by preferential sputtering, implantation, or chemical reaction.[43] In fact, in our earlier ptychography and STXM study of a Ga FIB ZnO/Al_2O_3 aerogel,[7] there was a large depletion of ZnO from the surface region (up to 2 μm into the $20 \times 20 \times 30$ μm^3 rectangular prism, sample D), which was ascribed to a higher sputtering rate of ZnO than Al_2O_3. In this study we prepared samples by both Ga FIB and Xe plasma FIB to investigate possible differences in sample damage effects between these methods. Figure S4 compares the lateral uniformity of the ratio of ZnO to Al_2O_3 in the first Xe plasma FIB (sample F) and the second GaFIB (sample G) samples, evaluated from STXM stack maps at the Zn L- and Al K-edges. In the case of the two Ga FIB samples, depletion of ZnO at the surface of the pillar was observed in both samples, but this was only over a depth of ~0.8 μm in the second preparation (Ga-FIB#2, Figure S4b,d), whereas the depletion occurred to a depth greater than 2 μm in the Ga-FIB#1 sample.[7] In the case of Xe plasma FIB, some ZnO depletion was observed (~240 nm in Xe-FIB #1 and ~200 nm in Xe-FIB#2 and -#3 (Figure S4a,c), but it is much less than that observed for Ga FIB. In fully dense materials, preferential sputtering is usually only seen at nanoscales since sputtering is a surface phenomenon. However, in the porous structure of the Al_2O_3 aerogel, the ions pass through many alternating layers of material and vacuum, which leads to a deeper sputtering effect. Ga is smaller than Xe so it tends to penetrate deeper, despite having less momentum. Therefore, preferential sputtering effects are expected to extend farther into the sample when using Ga rather than Xe FIB.

When the combined Zn L and Al K spectra of the rectangular prism Ga FIB#1 sample D were analyzed, it was important to include the elemental response of Ga to account for the implanted Ga.[7] However, for the Ga-FIB#2 sample G, where additional efforts were deployed to reduce damage effects, the fit to the combined Zn L- and Al K-edge spectra of the aerogel did not improve when a Ga reference signal was added, consistent with much lower levels of Ga implantation.

A second concern was possible radiation damage by the very high flux of X-rays used in making the ptychography measurements, which is ~2 orders of magnitude larger at the COSMIC beamline (~10^9 ph s^{-1} in ~60 nm diameter spot) than in conventional STXMs (~10^7 ph s^{-1} in ~30 nm diameter spot). The estimated total doses for the STXM and ptychography measurement of each sample are listed in Table S1. Figure S8 compares the Zn L- and Al K-edge spectra measured before and after the ptychography measurements on sample F. In terms of the spectral shapes there is reasonable agreement between the spectra recorded before and after ptychography at each edge. Unfortunately, because the spectra were measured from different positions on the pillar, it is not possible to check for preferential loss of ZnO.

4.2. 4D Chemical Structure. Our previous research[7] demonstrated the capability of soft X-ray chemically selective ptycho-tomography to derive structural and spectroscopic

information for both the Al_2O_3 aerogel scaffold and the ZnO ALD coating. However, the results were limited by the 2D (14 nm) and 3D (30 nm) spatial resolution. The higher spatial resolution of the COSMIC ptycho-tomography measurements provides new insights and can lead to a better understanding of optimal conditions for achieving more uniform, thin coatings of ZnO on Al_2O_3 aerogels. The structure of the ZnO ALD coating depends on the ALD parameters, such as coating temperature, deposition rate, and number of ALD cycles. This study examined how the 3D structure of the ZnO coating and its distribution on the Al_2O_3 aerogel framework change with the number of ALD deposition cycles. Figures 6a and 6b present volume renderings
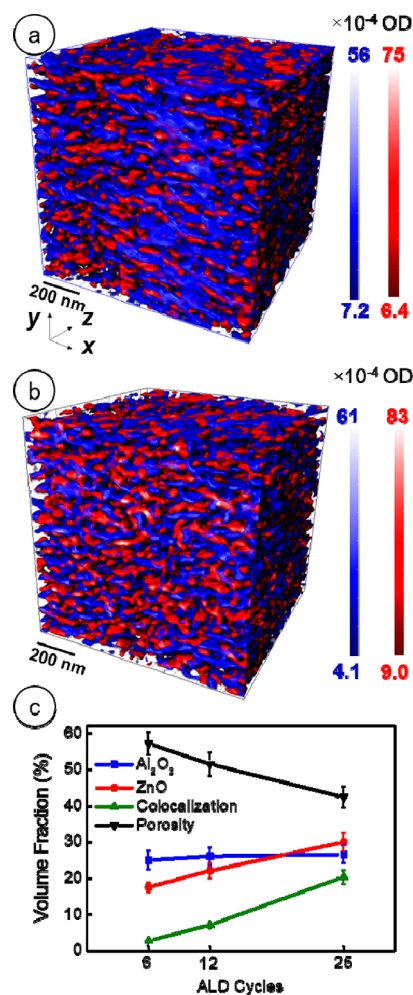

Figure 6. 3D chemical mapping of Al_2O_3 (blue) and ZnO (red) signals in a $1 \times 1 \times 1$ μm^3 volume from the tomographic reconstruction of ptychography maps of (a) the 6-cycle ALD-coated aerogel FIB sample, (Xe-FIB#2, sample F). Otsu thresholds of 7.3×10^{-4} (OD/voxel) for Al_2O_3 and 6.3×10^{-4} for ZnO were used. (b) The 12-cycle ALD-coated aerogel FIB sample, (Xe-FIB#3, sample H), Otsu thresholds of 4.72×10^{-4} (Al_2O_3) and 5.41×10^{-4} (ZnO). (c) Plot of the volume fraction of Al_2O_3, ZnO, colocalization (both Al_2O_3 and ZnO), and porosity as a function of ALD deposition cycles.

of the color-coded composite of the ZnO (red) and Al_2O_3 (blue) 3D distributions derived from ptycho-tomography on the 6-cycle (sample F) and 12-cycle (sample H) ZnO/Al_2O_3 aerogel samples. In each case the rendered volume is a $1 \times 1 \times 1$ μm^3 cube which was extracted from the center of the full volume to avoid artifacts from ion beam depletion of the ZnO at the edges

of the FIB samples. The voxel size is $5.2 \times 5.2 \times 5.2$ nm^3 for sample F and $4.8 \times 4.8 \times 4.8$ nm^3 for sample H. The volume fractions of the Al_2O_3 and ZnO components in the central 1 μm^3 volume unit for the 6-, 12-, and 25-cycle ALD materials, calculated by the bone analysis plugin in the Dragonfly software, are shown in Figure 6c. The volume fraction of pure Al_2O_3 is 25 ± 2% in all three types of ZnO-coated aerogels, while the ZnO increases roughly in proportion to the number of cycles, as expected. The quantitative volume fraction analysis determines the percent porosity as 100% minus the sum of the volumes that are exclusively Al_2O_3, ZnO, and those which have both signal of Al_2O_3 and ZnO ("colocalization") by using threshold values determined automatically by the Otsu method. The volume fractions of porosity in all three materials are significantly smaller than those predicted from the measured density of ~40 kg/m^3 of the Al_2O_3 aerogel substrate,[10,11] which corresponds to a porosity of ~98%. The difference is in part due to the presence of the ZnO ALD coating (which amounts to 20−30% of the volume, and thus should be added to the measured porosity volume, to compare to the porosity of the uncoated Al_2O_3 aerogel) and in part due to the finite 3D spatial resolution. The FSC analysis shows a spatial resolution of 9 nm in the 3D reconstruction of samples F and H, which means that any particle smaller than ~10 nm will be effectively 4 pixels when a 2D projection is derived from the 3D reconstruction and up to 8 voxels in 3D. This factor means that the solid material will be significantly overestimated relative to that which would be determined if the spatial resolution was only 1 nm. There are also cases where there are double layers or joints among different parts of the Al_2O_3 framework that are too close to be distinguished at ~9 nm spatial resolution, which thus introduces more volume assigned to solid material as opposed to pore space.

To quantitatively evaluate the spatial distributions of Al_2O_3 and ZnO as well as porosity in the three different aerogels, the relative concentration (RC)[44] of each species was calculated as a function of distance across the central 1 μm^3 volume unit (in the direction along the long axis of the FIB cylinder). RC is defined as the ratio of the amount of one species relative to the sum of all species, averaged over a number of voxels. Figures S9 and S10 present the results of this analysis for the 6-, 12-, and 25-cycle ALD samples. Figure 6c and Figure S9 show that the Al_2O_3 aerogel scaffold retains its shape and thus concentration in the selected volume unit for both materials, which makes the comparison of results for the three ALD coating deposition cycles more convincing. The average of "only ZnO" RC increases from 16 to 19 vol %, and the RC of colocalized voxels (ones with both Al_2O_3 and ZnO) increases from 2 to 7 vol % when the number of ALD deposition cycles increases from 6 to 12. This is accompanied by a decrease in the porosity fraction, as the ZnO partially fills the pore volume. Because the 3D spatial resolution of the chemically selective ptycho-tomography results for the 25-cycle ZnO/Al_2O_3 aerogel (sample A) is much lower (~30 nm, versus 9 nm for the 6- and 12-cycle data), detailed comparisons of this type cannot be extended to the 25-cycle sample. Instead for the remainder of this section, we discuss the effect of the number of ALD cycles on material structural properties based on data from only the 6- and 12-cycle samples.

To further evaluate the effect of the number of ALD deposition cycles on the structural properties of the ZnO/Al_2O_3 aerogels, individual ZnO crystals and Al_2O_3 scaffold sections were identified and segmented by the Dragonfly software by using the Feret diameter[45] as a measure of particle size. Here the Feret diameter[46] is used to identify individual

ZnO particles or Al_2O_3 scaffold sections. Because the 3D spatial resolution is ~9 nm, particles below 10 nm in Feret diameter were excluded from the segmentation. To distinguish different sizes of ZnO or Al_2O_3 sections, the object sizes are classified into two groups: (i) 10−40 nm and (ii) >40 nm. The results of this "Feret" analysis are presented in Figure 7a (Al_2O_3) and Figure
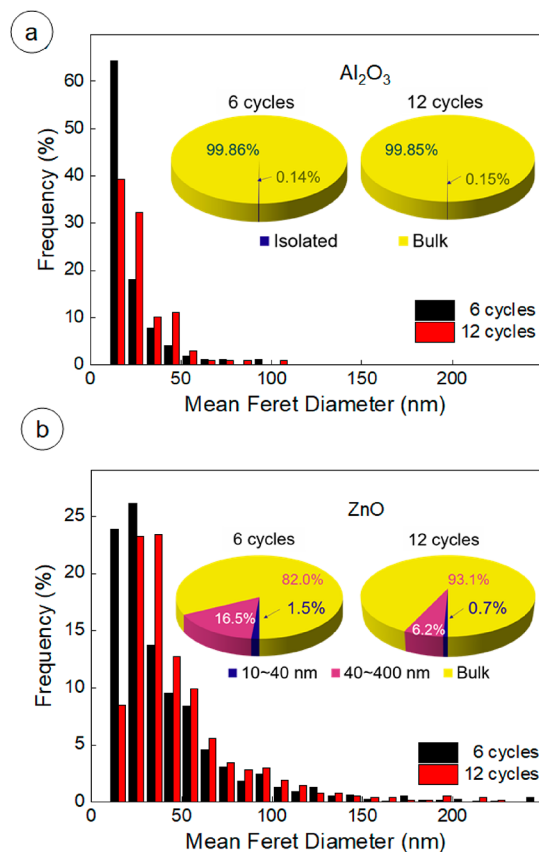

Figure 7. (a) Distribution of the Feret diameter (bar plot) of isolated individual Al_2O_3 entities in the aerogel material and their fraction of the entire Al_2O_3 volume for 6-cycle (Xe-FIB#2, sample F, black) and 12-cycle (Xe-FIB#3, sample H, red) ALD-coated aerogels in a selected (1 × 1 × 1 μm^3) volume of sample. (b) Distribution of Feret diameter (bar plot) of isolated individual ZnO crystals in the materials and their fraction of the entire ZnO volume in a selected (1 × 1 × 1 μm^3) volume of sample.

7b (ZnO). This analysis accounts for 99% of the porous Al_2O_3 framework for both the 6- and 12-cycle ALD samples. Figure 7b shows the frequency distribution histogram of Feret diameters of the segmented ZnO crystals/layers in the 6- and 12-cycle materials. The sizes of the ZnO crystals, which range from 10 to 150 nm, follow a log-normal distribution. The particle size distribution of ZnO in the 12-cycle sample is broader than that of the 6-cycle sample.

Size distributions of the ZnO volume maps were evaluated. Visualizations of the segmentation results for the ZnO coating are presented in Figure 8a−c for the 6-cycle and Figure 8d−f for the 12-cycle ALD ZnO/Al_2O_3 aerogel. The porous ZnO structures are shown in Figures 8a and 8c. The majority of the ZnO volume in the 6- and 12-cycle materials segments as a porous quasi-continuous network, which is intertwined with the Al_2O_3 scaffold. The rest of the ZnO consists of individual particles/crystals. The difference in the 3D distributions of the isolated ZnO crystals between the 6- and 12-cycle samples can
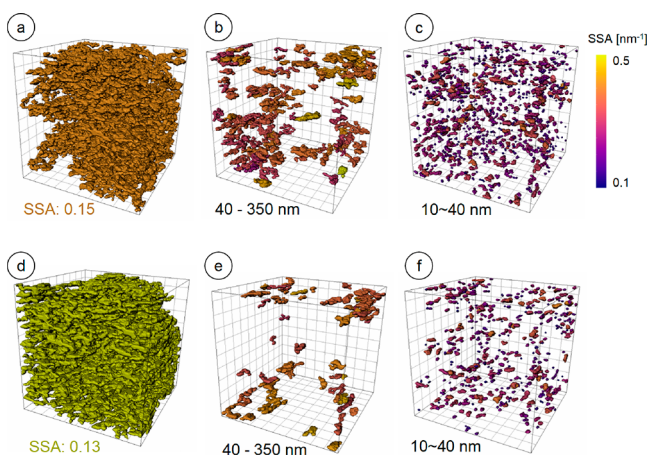
Figure 8. (a, b, c) 3D analysis of the sizes of the patchy ZnO coating in the $1 \times 1 \times 1 \ \mu m^3$ central volume unit of the 6-cycle ALD aerogel sample, (Xe-FIB#2, sample F): (a) segmented one-piece bulk ZnO 3D structure isolated from the selected volume in Figure 6a, (b) isolated ZnO layers (40−350 nm Feret diameter), and (c) isolated ZnO small crystals (10−40 nm Feret diameter). (d, e, f) 3D analysis of ZnO coating in the $1 \times 1 \times 1 \ \mu m^3$ volume unit of the 12-cycle ALD sample (Xe-FIB#3, sample H): (d) segmented one-piece bulk ZnO 3D structure, (e) isolated ZnO layers (40−350 nm Feret diameter), and (f) isolated ZnO small crystals (10−40 nm Feret diameter). Each display is color-coded by the specific surface area (SSA) scale in a purple-yellow color scheme (COSMIC, March and October 2019).

be seen by comparing Figures 8b and 8c with those of Figures 8d and 8e. The 3D ZnO particle size distributions in Figure 8a and the ZnO volume fraction analysis (Figure 8b) indicate there are more individual ZnO crystals in the 6-cycle sample (18% of the ZnO volume) than in the 12-cycle sample (7% of the ZnO volume). It is noted that many of the larger isolated particle aggregates (40−400 nm) are located at the surfaces and corners of the $(1 \ \mu m)^3$ central volume unit (see Figure 8b,d). We investigated whether this could be an artifact of the data processing, in particular the choice of the central $(1 \ \mu m)^3$ volume for analysis. To estimate possible bias from this effect, the size distribution and RC analysis was also performed on a $2 \times 2 \times 2 \ \mu m^3$ volume at the center of the measured area. The results of that analysis are very similar to those from the size distribution analysis of the $1 \times 1 \times 1 \ \mu m^3$ volume. There was a slight increase of bulk ZnO (∼0.2%) and bulk Al_2O_3 (∼0.05%) when the analyzed volume was increased (see Figure S11).

4.3. Relationship to ALD Optimization. While an ideal ALD process should result in conformal layer-by-layer growth,[47] under the growth conditions used, it seems that the ZnO did not wet the Al_2O_3 framework but instead aggregated into individual ZnO crystals. In the 25-cycle sample, the crystalline nature of these aggregates was revealed by high-resolution transmission electron microscopy.[7] With successive cycles, the ZnO nanocrystals grow, and some of the individual crystals join others to make a partially continuous structure. With increasing numbers of deposition cycles, a quasi-conformal, 3D network structure of ZnO gradually develops, as shown in Figures 7 and 8a,c. The apparent ZnO spatial distribution and degree of continuity of the ZnO coating on the aerogel scaffold do depend on the spatial resolution (compare the present results to those in ref 7) and also on the segmentation threshold. When the threshold is reduced, more spherical-shaped single ZnO crystals are observed in the longitudinal section. However, in many parts of the sample, they are still connected with each other when

examined in sections perpendicular to the long axis of the FIB samples (see Figure 4b). We note the observation of nonconformal growth and discrete ZnO crystals has important consequences for potential use of these ZnO ALD-coated Al_2O_3 aerogels as catalysts. Relative to a more uniform and thinly dispersed ZnO layer, the efficiency would be low in these materials, since the bulk of the ZnO would not contribute and only the surface of the 10−40 nm sized nanocrystals would be catalytically active.

The ZnO ALD-coated Al_2O_3 aerogel is an example of a customizable nanoporous material, in which the support and the coating can be optimized independently. Such systems have enormous potential for applications such as catalysis and energy storage. In such cases surface area is a critical parameter. The specific surface area (SSA) is a property of solids defined as the total surface area of a material per unit volume.[48] It is a physical value which has particular importance for adsorption, heterogeneous catalysis, and reactions on surfaces. The SSA corresponding to the segmented components was also evaluated by the Dragonfly software. The SSA for the Al_2O_3 framework is very similar for the 6- and 12-cycle samples, with an average of $0.131 \pm 0.002 \ nm^{-1}$ for the 6-cycle sample and $0.134 \pm 0.002 \ nm^{-1}$ for the 12-cycle sample. However, the SSA of the ZnO samples is significantly different for the 6- and 12-cycle samples. Figure 8 displays SSA distributions color-coded by their corresponding calculated SSA (in nm^{-1}). The SSA of ZnO in both materials has a wide distribution, ranging from small individual particles to larger layers. Compared with the large layers or porous bulk (0.13−0.28 nm^{-1}) for both 6 and 12 cycles, the small individual particles have a larger specific surface area per unit volume (0.28−0.54 nm^{-1}), which indicates the 6-cycle ALD material has a larger net surface area of ZnO than the 12-cycle material (see Figure S12). The quantitative results indicate that when compared to the 6-cycle samples, the ZnO in the 12-cycle sample is more uniformly distributed. The porous bulk ZnO structure in the 6-cycle sample has a mean SSA of $0.153 \pm 0.003 \ nm^{-1}$ (color-coded in Figure 8a), while the porous bulk ZnO in the 12-cycle sample has a mean SSA of $0.134 \pm 0.002 \ nm^{-1}$ (color-coded in Figure 8d). In addition, the 6-cycle sample contains a higher proportion and quantity of individual crystals and larger layers with a higher specific surface area than found in the 12-cycle sample, as shown in Figure 8.

Table 1 reports the calculated volume fraction, surface area, and specific surface area (SSA) of Al_2O_3 and ZnO inside the selected $(1 \times 1 \times 1 \ \mu m^3)$ volume unit of the 6- and 12-cycle ALD samples. The volume and surface area of the Al_2O_3 component are similar for the 6- and 12-cycle samples. In contrast, the volume fraction of ZnO increased by 26% as the number of ALD deposition cycles increased from 6 to 12. However, the surface area increased by only 6.5%. With additional deposition cycles, the small individual crystals and thin layers grow thicker, which decreases the SSA. The SSA of ZnO in the 12-cycle sample (0.13 $\pm$ 0.01 nm^{-1}) is smaller than that of the 6-cycle sample (0.16 $\pm$ 0.01 nm^{-1}). The uncertainty in the derived SSA values was evaluated by comparing the SSA in the larger $(2 \times 2 \times 2 \ \mu m^3)$ volume by using the same analysis method (see Table S3). The individual ZnO crystals in the 12-cycle sample have a smaller SSA distribution than the 6-cycle one (see Figure S12). These results show that increasing the number of ALD deposition cycles introduces more deposited ZnO. However, the change in surface area not only is related to the amount of ZnO deposited but also depends on the 3D structure of the aerogel and the nature of the first cycles of ALD coating.

Table 1. Volume Fraction, Surface Area, and Specific Surface Area (SSA) of Al_2O_3 and ZnO Components Inside the Central $1 \times 1 \times 1\ \mu m^3$ Volume of the 6- and 12-Cycle ZnO/Al_2O_3 Aerogel Samples

sample	6-cycle ALD[a]		12-cycle ALD[b]	
component	Al_2O_3	ZnO	Al_2O_3	ZnO
volume ($\times 10^8$ nm^3)	2.51 ± 0.03	1.76 ± 0.03	2.62 ± 0.03	2.22 ± 0.03
surface area ($\times 10^7$ nm^2)	3.31 ± 0.06	2.79 ± 0.03	3.50 ± 0.05	2.97 ± 0.03
SSA ($\times 10^{-1}$ nm^{-1})	1.31 ± 0.01	1.59 ± 0.02	1.34 ± 0.01	1.35 ± 0.01

[a]Otsu thresholds used for segmenting the 6-cycle ALD sample F: 7.3×10^{-4} (Al_2O_3) and 6.3×10^{-4} (ZnO). [b]Otsu thresholds used for segmenting the 12-cycle ALD sample H: 4.7×10^{-4} (Al_2O_3) and 5.4×10^{-4} (ZnO).

Pore connectivity and effective diffusivity are important features of nanoporous materials for applications in high-performance adsorption, energy conversion, and catalysis.[10,11] A quantitative analysis of the pore network and pore connectivity in the 6- and 12-cycle samples has been performed by using the Dragonfly software.[32] The pore networks and isolated pores were extracted and derived by using custom MATLAB code and Dragonfly by inverting the intensity of the sum of the Al_2O_3 and ZnO 3D volume maps. Figure 9 shows segmentations of the 3D
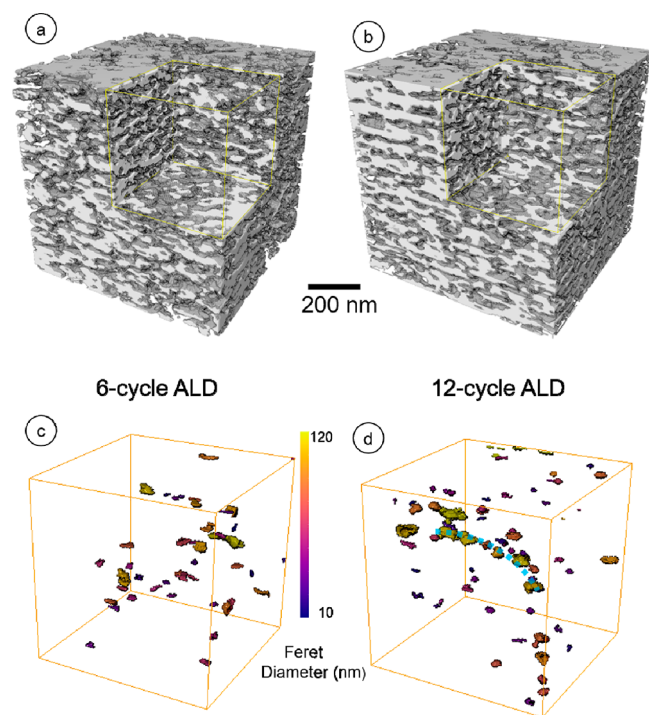

Figure 9. Volume rendered display of 3D porosity in the in $1 \times 1 \times 1$ μm^3 volume unit of (a) the 6-cycle (Xe-FIB#2, sample F) and (b) 12-cycle (Xe-FIB#3, sample H) ALD-coated Al_2O_3 aerogel sample. The segmented one-piece continuous 3D-mesh pore structure is displayed on a gray scale. (c, d) Isolated small pores in the cut-out $0.5^3\ \mu m^3$ volume (indicated by the yellow box plotted in (a, b)) colored by their Feret diameter in a purple-yellow color scheme. A set of isolated pores arranged in a "tube" inside the 12-cycle sample are marked by a blue dashed line in (d).

pore network in the 6- and 12-cycle ALD coating aerogel samples, corresponding to the cut-out $1 \times 1 \times 1\ \mu m^3$ volume unit in Figure 6. The majority of the pore structure consists of continuous connected networks in both samples: $99.4 \pm 0.2\%$ of the total pore volume in the 6-cycle sample and $98.9 \pm 0.2\%$ in the 12-cycle sample, as shown in Figure 9a,b displayed in a gray scale. The 3D distributions of isolated pores are displayed in Figure 9c,d, by using a color scheme that relates to their size (Feret diameter). The 6-cycle sample has better pore connectivity and thus more effective diffusivity with a lower quantity and smaller size of isolated pores in the unit volume. Some of the isolated pores in the 12-cycle sample are arranged in a "tube" (marked by a blue dashed line in Figure 9d) which suggests that originally open channels in the uncoated aerogel are being blocked by a thicker ZnO coating.

Movie S2 is a fly through the interior structure of the $1 \times 1 \times 1$ μm^3 central volume of sample H.

Movie S3 is a volume rendering of the pore network extracted from the $1 \times 1 \times 1\ \mu m^3$ central volume of sample H. This movie gives a good sense of the extent of pore connectivity in the 12-cycle sample.

5. CONCLUSION

Chemically selective ptycho-tomography was performed on a set of ZnO ALD-coated nanoporous Al_2O_3 aerogel samples. These materials are representative of a class of designer catalysts in which the nanoporous support is prepared separately from the active nanoscale catalyst material, which is subsequently introduced by ALD, thereby allowing independent optimization of the morphology, chemistry, and spatial distribution of the support and catalyst. FRC analysis of 2D ptychographic images and single-component maps measured with the new ALS COSMIC dedicated ptychography beamline give a 2D half-period spatial resolution below 7 nm while FSC analysis indicates a 3D half-period resolution below 9 nm. The higher coherent flux at the COSMIC beamline has provided a clearer visualization of the spatial distribution of the ZnO ALD coating on the Al_2O_3 porous framework. This is a significant enhancement relative to our previous chemically selective ptycho-tomography results, measured earlier on the same type of material at ALS bend magnet BL 5.3.2.1.[7]

In addition to illustrating the exceptional performance of the ALS COSMIC ptychography facility, this study confirmed the previous conclusion that the ZnO coating does not uniformly cover the surface of the Al_2O_3 aerogel framework. It has provided information that may contribute to optimization of the ALD process parameters with the ultimate goal of identifying those that provide the highest surface area per unit deposited mass of ZnO.

■ ASSOCIATED CONTENT

ⓢ Supporting Information

The Supporting Information is available free of charge at https://pubs.acs.org/doi/10.1021/acsanm.0c02924.

Scheme S1, Figures S1−S12, and Tables S1−S3 (PDF)

Movie S1 (MP4)

Movie S2 (MP4)

Movie S3 (MP4)

■ AUTHOR INFORMATION

Corresponding Author

Adam P. Hitchcock — *Department Chemistry & Chemical Biology, McMaster University, Hamilton, ON L8S 4M1, Canada;* ⊙ orcid.org/0000-0002-1598-7886; Phone: +1 905 525-9140; Email: aph@mcmaster.ca

Authors

Hao Yuan — *Department Chemistry & Chemical Biology, McMaster University, Hamilton, ON L8S 4M1, Canada*

Hui Yuan — *Canadian Centre for Electron Microscopy, McMaster University, Hamilton, ON L8S 4M1, Canada*

Travis Casagrande — *Canadian Centre for Electron Microscopy, McMaster University, Hamilton, ON L8S 4M1, Canada*

David Shapiro — *Advanced Light Source, Lawrence Berkeley National Laboratory, Berkeley, California 94720, United States*

Young-Sang Yu — *Advanced Light Source, Lawrence Berkeley National Laboratory, Berkeley, California 94720, United States*

Bjoern Enders — *National Energy Research Scientific Computing Center, Lawrence Berkeley National Laboratory, Berkeley, California 94720, United States; Department of Physics, University of California, Berkeley, Berkeley, California 94720, United States*

Jonathan R. I. Lee — *Lawrence Livermore National Laboratory, Livermore, California 94550, United States*

Anthony van Buuren — *Lawrence Livermore National Laboratory, Livermore, California 94550, United States*

Monika M. Biener — *Lawrence Livermore National Laboratory, Livermore, California 94550, United States;* ⊙ orcid.org/0000-0001-7289-5905

Stuart A. Gammon — *Lawrence Livermore National Laboratory, Livermore, California 94550, United States*

Theodore F. Baumann — *Lawrence Livermore National Laboratory, Livermore, California 94550, United States*

Complete contact information is available at:
https://pubs.acs.org/10.1021/acsanm.0c02924

Author Contributions

Hao.Y., A.P.H., J.R.I.L., and T.V.B. conceived and planned the experiment. D.A.S., Y.-S.Y., and B.E. developed experimental equipment and ptychographic reconstruction codes. The ALD-coated aerogel samples were fabricated by M.M.B., S.A.G., and T.F.B. Hui.Y. and T.C. prepared the FIB samples. Hao.Y. and A.P.H. performed the data analysis and spectral interpretation. Hao.Y. and A.P.H. prepared the manuscript, which incorporates critical input from all authors.

Notes

The authors declare no competing financial interest.

■ REFERENCES

(1) Biener, J.; Baumann, T. F.; Wang, Y.; Nelson, E. J.; Kucheyev, S. O.; Hamza, A. V.; Kemell, M.; Ritala, M.; Leskelä, M. Ruthenium/Aerogel Nanocomposites via Atomic Layer Deposition. *Nanotechnology* **2007**, *18* (5), 055303.

(2) Biener, J.; Stadermann, M.; Suss, M.; Worsley, M. A.; Biener, M. M.; Rose, K. A.; Baumann, T. F. Advanced Carbon Aerogels for Energy Applications. *Energy Environ. Sci.* **2011**, *4* (3), 656−667.

(3) Baji, Z.; Lábadi, Z.; Horváth, Z. E.; Molnár, G.; Volk, J.; Bársony, I.; Barna, P. Nucleation and Growth Modes of ALD ZnO. *Cryst. Growth Des.* **2012**, *12* (11), 5615−5620.

(4) Torruella, P.; Arenal, R.; De La Peña, F.; Saghi, Z.; Yedra, L.; Eljarrat, A.; López-Conesa, L.; Estrader, M.; López-Ortega, A.; Salazar-Alvarez, G.; Nogués, J.; Ducati, C.; Midgley, P. A.; Peiró, F.; Estradé, S. 3D Visualization of the Iron Oxidation State in FeO/Fe₃O₄ Core-Shell Nanocubes from Electron Energy Loss Tomography. *Nano Lett.* **2016**, *16* (8), 5068−5073.

(5) Shapiro, D. A.; Yu, Y. S.; Tyliszczak, T.; Cabana, J.; Celestre, R.; Chao, W.; Kaznatcheev, K.; Kilcoyne, A. L. D.; Maia, F.; Marchesini, S.; Meng, Y. S.; Warwick, T.; Yang, L. L.; Padmore, H. A. Chemical Composition Mapping with Nanometre Resolution by Soft X-Ray Microscopy. *Nat. Photonics* **2014**, *8* (10), 765−769.

(6) Hitchcock, A. P. Soft X-Ray Imaging and Spectromicroscopy. In *Handbook of Nanoscopy*; Wiley-VCH Verlag GmbH & Co. KGaA: Weinheim, Germany, 2012; Vol. 2, pp 745−791.

(7) Wu, J.; Zhu, X.; Shapiro, D. A.; Lee, J. R. I.; Van Buuren, T.; Biener, M. M.; Gammon, S. A.; Li, T. T.; Baumann, T. F.; Hitchcock, A. P. Four-Dimensional Imaging of ZnO-Coated Alumina Aerogels by Scanning Transmission X-Ray Microscopy and Ptychographic Tomography. *J. Phys. Chem. C* **2018**, *122* (44), 25374−25385.

(8) Shapiro, D. A.; Celestre, R.; Enders, B.; Joseph, J.; Krishnan, H.; Marcus, M. A.; Nowrouzi, K.; Padmore, H.; Park, J.; Warwick, A.; Yu, Y.-S. The COSMIC Imaging Beamline at the Advanced Light Source: A New Facility for Spectro-Microscopy of Nano-Materials. *Microsc. Microanal.* **2018**, *24* (S2), 8−11.

(9) Marchesini, S.; Krishnan, H.; Daurer, B. J.; Shapiro, D. A.; Perciano, T.; Sethian, J. A.; Maia, F. R. N. C. SHARP: A Distributed GPU-Based Ptychographic Solver. *J. Appl. Crystallogr.* **2016**, *49* (4), 1245−1252.

(10) Poco, J. F.; Satcher, J. H.; Hrubesh, L. W. Synthesis of High Porosity, Monolithic Alumina Aerogels. *J. Non-Cryst. Solids* **2001**, *285* (1−3), 57−63.

(11) Baumann, T. F.; Gash, A. E.; Chinn, S. C.; Sawvel, A. M.; Maxwell, R. S.; Satcher, J. H. Synthesis of High-Surface-Area Alumina Aerogels without the Use of Alkoxide Precursors. *Chem. Mater.* **2005**, *17* (2), 395−401.

(12) Bassim, N. D.; De Gregorio, B. T.; Kilcoyne, A. L. D.; Scott, K.; Chou, T.; Wirick, S.; Cody, G.; Stroud, R. M. Minimizing Damage

during FIB Sample Preparation of Soft Materials. *J. Microsc.* **2012**, *245* (3), 288−301.

(13) Schmied, R.; Chernev, B.; Trimmel, G.; Plank, H. New Possibilities for Soft Matter Applications: Eliminating Technically Induced Thermal Stress during FIB Processing. *RSC Adv.* **2012**, *2* (17), 6932−6938.

(14) Orthacker, A.; Schmied, R.; Chernev, B.; Fröch, J. E.; Winkler, R.; Hobisch, J.; Trimmel, G.; Plank, H. Chemical Degradation and Morphological Instabilities during Focused Ion Beam Prototyping of Polymers. *Phys. Chem. Chem. Phys.* **2014**, *16* (4), 1658−1666.

(15) Schmied, R.; Fröch, J. E.; Orthacker, A.; Hobisch, J.; Trimmel, G.; Plank, H. A Combined Approach to Predict Spatial Temperature Evolution and Its Consequences during FIB Processing of Soft Matter. *Phys. Chem. Chem. Phys.* **2014**, *16* (13), 6153−6158.

(16) Shapiro, D. A.; Celestre, R.; Denes, P.; Farmand, M.; Joseph, J.; Kilcoyne, A. L. D.; Marchesini, S.; Padmore, H.; Venkatakrishnan, S. V.; Warwick, T.; Yu, Y. S. Ptychographic Imaging of Nano-Materials at the Advanced Light Source with the Nanosurveyor Instrument. *J. Phys.: Conf. Ser.* **2017**, *849*, 012028.

(17) Farmand, M.; Celestre, R.; Denes, P.; Kilcoyne, A. L. D.; Marchesini, S.; Padmore, H.; Tyliszczak, T.; Warwick, T.; Shi, X.; Lee, J.; Yu, Y. S.; Cabana, J.; Joseph, J.; Krishnan, H.; Perciano, T.; Maia, F. R. N. C.; Shapiro, D. A. Near-Edge X-Ray Refraction Fine Structure Microscopy. *Appl. Phys. Lett.* **2017**, *110* (6), 063101.

(18) Celestre, R.; Nowrouzi, K.; Shapiro, D. A.; Denes, P.; Joseph, J. M.; Schmid, A.; Padmore, H. A. Nanosurveyor 2: A Compact Instrument for Nano-Tomography at the Advanced Light Source. *J. Phys.: Conf. Ser.* **2017**, *849*, 012047.

(19) Shapiro, D.; Roy, S.; Celestre, R.; Chao, W.; Doering, D.; Howells, M.; Kevan, S.; Kilcoyne, D.; Kirz, J.; Marchesini, S.; Seu, K. A.; Schirotzek, A.; Spence, J.; Tyliszczak, T.; Warwick, T.; Voronov, D.; Padmore, H. A. Development of Coherent Scattering and Diffractive Imaging and the COSMIC Facility at the Advanced Light Source. *J. Phys.: Conf. Ser.* **2013**, *425*, 192011.

(20) Jacobsen, C.; Wirick, S.; Flynn, G.; Zimba, C. Soft X-Ray Spectroscopy from Image Sequences with Sub-100 Nm Spatial Resolution. *J. Microsc.* **2000**, *197* (2), 173−184.

(21) Wang, M.; Ren, F.; Zhou, J.; Cai, G.; Cai, L.; Hu, Y.; Wang, D.; Liu, Y.; Guo, L.; Shen, S. N Doping to ZnO Nanorods for Photoelectrochemical Water Splitting under Visible Light: Engineered Impurity Distribution and Terraced Band Structure. *Sci. Rep.* **2015**, *5* (1), 12925.

(22) Dadlani, A. L.; Trejo, O.; Acharya, S.; Torgersen, J.; Petousis, I.; Nordlund, D.; Sarangi, R.; Schindler, P.; Prinz, F. B. Exploring the Local Electronic Structure and Geometric Arrangement of ALD Zn(O,S) Buffer Layers Using X-Ray Absorption Spectroscopy. *J. Mater. Chem. C* **2015**, *3* (47), 12192−12198.

(23) Dadlani, A.; Acharya, S.; Trejo, O.; Nordlund, D.; Peron, M.; Razavi, J.; Berto, F.; Prinz, F. B.; Torgersen, J. Revealing the Bonding Environment of Zn in ALD Zn(O,S) Buffer Layers through X-Ray Absorption Spectroscopy. *ACS Appl. Mater. Interfaces* **2017**, *9* (45), 39105−39109.

(24) Shimizu, K.; Kato, Y.; Yoshida, H.; Satsuma, A.; Hattori, T.; Yoshida, T. Al K-Edge XANES Study for the Quantification of Aluminium Coordinations in Alumina. *Chem. Commun.* **1999**, No. 17, 1681−1682.

(25) Mogi, M.; Yamamoto, T.; Mizoguchi, T.; Tatsumi, K.; Yoshioka, S.; Kameyama, S.; Tanaka, I.; Adachi, H. Theoretical Investigation of Al K-Edge X-Ray Absorption Spectra of Al, AlN and Al_2O_3. *Mater. Trans.* **2004**, *45* (7), 2031−2034.

(26) Neuville, D. R.; Cormier, L.; Roux, J.; Henderson, G. S.; De Ligny, D.; Flank, A. M.; Lagarde, P. Investigation of Aluminate and Al_2O_3 Crystals and Melts at High Temperature Using XANES Spectroscopy. *AIP Conf. Proc.* **2006**, *882*, 419−421.

(27) Nakanishi, K.; Ohta, T. Verification of the FEFF Simulations to K-Edge XANES Spectra of the Third Row Elements. *J. Phys.: Condens. Matter* **2009**, *21* (10), 104214.

(28) Altman, A. B.; Pemmaraju, C. D.; Alayoglu, S.; Arnold, J.; Booth, C. H.; Braun, A.; Bunker, C. E.; Herve, A.; Minasian, S. G.; Prendergast, D.; Shuh, D. K.; Tyliszczak, T. Chemical and Morphological Inhomogeneity of Aluminum Metal and Oxides from Soft X-Ray Spectromicroscopy. *Inorg. Chem.* **2017**, *56* (10), 5710−5719.

(29) Henke, B. L.; Gullikson, E. M.; Davis, J. C. X-Ray Interactions: Photoabsorption, Scattering, Transmission and Reflection E= 50− 30,000 EV, Z= 1−92. *At. Data Nucl. Data Tables* **1993**, *54* (2).

(30) Hitchcock, A. P. AXis2000 is written in Interactive Data Language (IDL). It is available free for noncommercial use from http// unicorn.mcmaster.ca/aXis2000.html, 2008.

(31) Denes, P.; Doering, D.; Padmore, H. A.; Walder, J. P.; Weizeorick, J. A Fast, Direct x-Ray Detection Charge-Coupled Device. *Rev. Sci. Instrum.* **2009**, *80* (8), 083302.

(32) *Dragonfly 3.6 [Computer Software]*; Object Research Systems (ORS) Inc.: Montreal, Canada, 2018.

(33) Thévenaz, P.; Ruttimann, U. E.; Unser, M. A Pyramid Approach to Subpixel Registration Based on Intensity. *IEEE Trans. Image Process.* **1998**, *7* (1), 27−41.

(34) Wu, J.; Lerotic, M.; Collins, S.; Leary, R.; Saghi, Z.; Midgley, P.; Berejnov, S.; Susac, D.; Stumper, J.; Singh, G.; Hitchcock, A. P. Optimization of Three-Dimensional (3D) Chemical Imaging by Soft X-Ray Spectro-Tomography Using a Compressed Sensing Algorithm. *Microsc. Microanal.* **2017**, *23* (5), 951−966.

(35) Bhardwaj, R.; Bharti, A.; Singh, J. P.; Chae, K. H.; Goyal, N.; Gautam, S. Structural and Electronic Investigation of ZnO Nanostructures Synthesized under Different Environments. *Heliyon* **2018**, *4* (4), No. e00594.

(36) Li, D.; Bancroft, G. M.; Fleet, M. E.; Feng, X. H.; Pan, Y. Al K-Edge XANES Spectra of Aluminosilicate Minerals. *Am. Mineral.* **1995**, *80* (5−6), 432−440.

(37) Aramburo, L. R.; Liu, Y.; Tyliszczak, T.; De Groot, F. M. F.; Andrews, J. C.; Weckhuysen, B. M. 3D Nanoscale Chemical Imaging of the Distribution of Aluminum Coordination Environments in Zeolites with Soft X-Ray Microscopy. *ChemPhysChem* **2013**, *14* (3), 496−499.

(38) Henderson, G. S.; De Groot, F. M. F.; Moulton, B. J. A. X-Ray Absorption near-Edge Structure (XANES) Spectroscopy. *Rev. Mineral. Geochem.* **2014**, *78* (1), 75−138.

(39) Otsu, N. A Threshold Selection Method from Gray-Level Histograms. *IEEE Trans. Syst. Man. Cybern.* **1979**, *9* (1), 62−66.

(40) Banterle, N.; Bui, K. H.; Lemke, E. A.; Beck, M. Fourier Ring Correlation as a Resolution Criterion for Super-Resolution Microscopy. *J. Struct. Biol.* **2013**, *183* (3), 363−367.

(41) Van Heel, M.; Schatz, M. Fourier Shell Correlation Threshold Criteria. *J. Struct. Biol.* **2005**, *151* (3), 250−262.

(42) Yu, Y. S.; Farmand, M.; Kim, C.; Liu, Y.; Grey, C. P.; Strobridge, F. C.; Tyliszczak, T.; Celestre, R.; Denes, P.; Joseph, J.; Krishnan, H.; Maia, F. R. N. C.; Kilcoyne, A. L. D.; Marchesini, S.; Leite, T. P. C.; Warwick, T.; Padmore, H.; Cabana, J.; Shapiro, D. A. Three-Dimensional Localization of Nanoscale Battery Reactions Using Soft X-Ray Tomography. *Nat. Commun.* **2018**, *9* (1), 1−7.

(43) Frey, L.; Lehrer, C.; Ryssel, H. Nanoscale Effects in Focused Ion Beam Processing. *Appl. Phys. A: Mater. Sci. Process.* **2003**, *76*, 1017−1023.

(44) Yang, F.; Liu, Y.; Martha, S. K.; Wu, Z.; Andrews, J. C.; Ice, G. E.; Pianetta, P.; Nanda, J. Nanoscale Morphological and Chemical Changes of High Voltage Lithium-Manganese Rich NMC Composite Cathodes with Cycling. *Nano Lett.* **2014**, *14* (8), 4334−4341.

(45) Walton, W. H. Feret's Statistical Diameter as a Measure of Particle Size [2]. *Nature* **1948**, *162*, 329−330.

(46) Merkus, H. G. *Particle Size Measurements: Fundamentals, Practice, Quality*; Springer Science & Business Media: 2009; Vol. *17*.

(47) Mallick, B. C.; Hsieh, C.-T.; Yin, K.-M.; Gandomi, Y. A.; Huang, K.-T. Review—On Atomic Layer Deposition: Current Progress and Future Challenges. *ECS J. Solid State Sci. Technol.* **2019**, *8* (4), N55−N78.

(48) Amador, C.; Martin de Juan, L. Strategies for Structured Particulate Systems Design. *Comput.-Aided Chem. Eng.* **2016**, *39*, 509−579.